

## Electric Control of Dirac Quasiparticles by Spin-Orbit Torque in an Antiferromagnet

L. Šmejkal,<sup>1,2,3</sup> J. Železný,<sup>4,1</sup> J. Sinova,<sup>2,1</sup> and T. Jungwirth<sup>1,5</sup>

<sup>1</sup>*Institute of Physics, Academy of Sciences of the Czech Republic, Cukrovarnická 10, 162 53 Praha 6, Czech Republic*

<sup>2</sup>*Institut für Physik, Johannes Gutenberg Universität Mainz, D-55099 Mainz, Germany*

<sup>3</sup>*Faculty of Mathematics and Physics, Charles University in Prague, Ke Karlovu 3, 121 16 Prague 2, Czech Republic*

<sup>4</sup>*Max Planck Institute for Chemical Physics of Solids, Nöthnitzer Strasse 40, D-01187 Dresden, Germany*

<sup>5</sup>*School of Physics and Astronomy, University of Nottingham, Nottingham NG7 2RD, United Kingdom*

(Received 27 October 2016; published 6 March 2017)

Spin orbitronics and Dirac quasiparticles are two fields of condensed matter physics initiated independently about a decade ago. Here we predict that Dirac quasiparticles can be controlled by the spin-orbit torque reorientation of the Néel vector in an antiferromagnet. Using CuMnAs as an example, we formulate symmetry criteria allowing for the coexistence of topological Dirac quasiparticles and Néel spin-orbit torques. We identify the nonsymmorphic crystal symmetry protection of Dirac band crossings whose on and off switching is mediated by the Néel vector reorientation. We predict that this concept verified by minimal model and density functional calculations in the CuMnAs semimetal antiferromagnet can lead to a topological metal-insulator transition driven by the Néel vector and to the topological anisotropic magnetoresistance.

DOI: [10.1103/PhysRevLett.118.106402](https://doi.org/10.1103/PhysRevLett.118.106402)

In 2004, the spin Hall effect was observed in GaAs [1–3] and one-atom-thick flakes of graphene were isolated [4,5]. The former discovery marked the dawn of the field of spin orbitronics, in which the relativistic conversion between linear momentum and spin angular momentum of conducting electrons has provided new physical concepts for spintronics devices. These include the spin-orbit torque (SOT), which has opened the path to reliable and fast information writing in a ferromagnetic random access memory [6,7] and also to efficient means of the electrical switching of an antiferromagnet (AF) by the Néel SOT [8,9]. Independently, the discovery of graphene initiated intense research of Dirac fermion quasiparticles, in particular, as a new platform for exploring topological phases [10] in condensed matter. The field includes topological insulators, semimetals, or superconductors, which host a family of quasiparticles mimicking different flavors of fermions from relativistic particle physics [11–13]. More recently, novel phenomena have been discovered at the intersection of spin orbitronics, Dirac quasiparticles, and topological phases, such as the quantum spin Hall effect and the quantum anomalous Hall effect in nonmagnetic and magnetic topological insulators [14–19]. Dirac quasiparticles exhibiting a strong spin-momentum locking are also considered for enhancing the efficiency of the SOT control of magnetic moments in ferromagnetic topological insulator heterostructures [20].

In this Letter, we close the loop of synergies between the fields of spin orbitronics and topological Dirac quasiparticles by proposing a scheme for the electric control of Dirac band crossings via the Néel SOT in AFs. Our work addresses the outstanding problem of finding efficient means for controlling Dirac quasiparticles by external

fields which may provide the desired tools for the experimental research and future practical applications in microelectronics [21]. In a specific example of the semimetal CuMnAs AF [9,22–24], we demonstrate that the Néel vector orientation is a suitable degree of freedom that can mediate on and off switching of the symmetry protection of Dirac band crossings. Based on this, we also predict the topological metal-insulator transition (MIT) and the topological anisotropic magnetoresistance (AMR) in Dirac semimetal AFs. Our results suggest a generic strategy for designing large topological magnetotransport effects for spintronics.

Dirac quasiparticles and the Néel SOT can coexist because of the serendipitous overlap of the key symmetry requirements. We illustrate this in examples shown in Figs. 1(a) and 1(b) of the graphene lattice representing the Dirac systems [25] and the tetragonal CuMnAs crystal where the Néel SOT has been experimentally verified [9]. (i) The two-Mn-site primitive cell of CuMnAs favors band crossings in analogy with the two-C-site graphene lattice. (ii) In the paramagnetic phase, CuMnAs has time reversal ( $\mathcal{T}$ ) and space inversion ( $\mathcal{P}$ ) symmetries. It guarantees that each band is double degenerate forming a Kramers pair, in analogy to graphene. In the AF phase, this degeneracy is not lifted because the combined  $\mathcal{PT}$  symmetry is preserved, although the  $\mathcal{T}$  symmetry and the  $\mathcal{P}$  symmetry are each broken [24,26–28]. This highlights antiferromagnetism as the favorable type of magnetic order for controlling Dirac quasiparticles. (iii) Finally, the combined  $\mathcal{PT}$  symmetry also allows for the efficient SOT reorientation of the Néel vector [8,29]. Because the  $A$  and  $B$  Mn sites in the CuMnAs primitive cell are noncentrosymmetric inversion partners, a nonequilibrium spin-polarization  $\delta s_{A,B}$  with

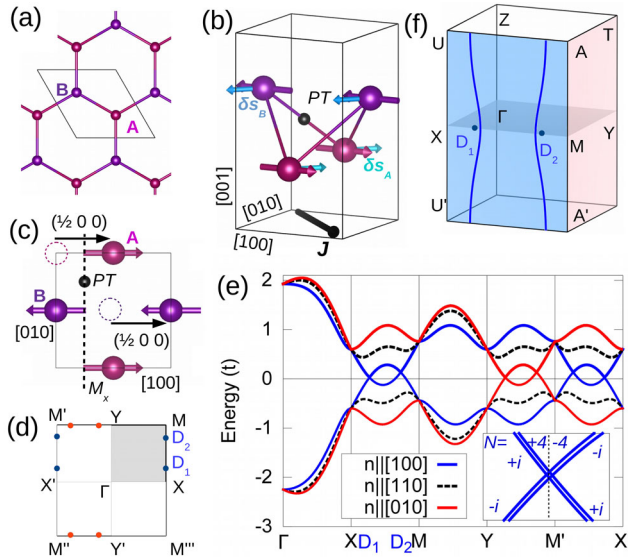


FIG. 1. (a) Graphene two- $A$ ,  $B$ -sublattice crystal. (b) Minimal two- $A$ ,  $B$ -sublattice AF with the nonsymmorphic symmetry extracted from CuMnAs. The two magnetic sublattices are connected by the  $\mathcal{PT}$  symmetry center marked by the black ball, and they are noncentrosymmetric. This allows for the nonzero staggered nonequilibrium spin polarizations  $\delta s_{A,B}$  induced by the current  $\mathbf{J}$ , which facilitates the manipulation of the Néel vector. (c) Top view of our quasi-2D-AF model highlighting the nonsymmorphic glide mirror plane  $\mathcal{G}_x$  (see text). (d) 2D Brillouin zone (BZ) projection with the Dirac point (DP) positions for  $\mathbf{n} \parallel [100]$  along the  $MX$  axis (blue), while for  $\mathbf{n} \parallel [010]$  along the  $M'Y$  axis (red). (e) Band dispersion of our minimal AF model illustrating the control of the DPs and topological indexes of the DP  $D_1$  in the inset (for the sake of clarity, the degenerate bands are slightly shifted). (f) 3D model BZ with the Dirac nodal lines [the colors of the planes protected for a given Néel vector orientation correspond to (d),(e)].

opposite sign on the two sites is generated by an electrical current  $\mathbf{J}$  [see Fig. 1(b)] [8]. This applies to both the paramagnetic and the AF phase above and below the Néel temperature of CuMnAs. Moreover, in the AF phase, the inversion partner  $A$  and  $B$  sites are occupied by oppositely oriented Mn magnetic moments (hence, the combined  $\mathcal{PT}$  symmetry). The current-induced nonequilibrium spin polarization and the equilibrium AF moments are, therefore, both staggered and commensurate. In combination with the exchange interaction that couples them, the resulting current-induced Néel SOT can efficiently reorient the Néel vector [8,9].

An additional crystal symmetry is now needed to mediate the dependence of Dirac quasiparticles on the Néel vector orientation. In graphene, there is no symmetry that protects the fourfold degeneracy of Dirac crossings of two Kramers pair bands in the presence of spin-orbit coupling (SOC) [14]. Inspired by recent predictions of the symmetry protection of band crossings in Dirac semimetals [30–32], we identify nonsymmorphic symmetries that can be turned on and off

by reorienting the Néel vector in CuMnAs and by this can close and open a gap at the Dirac crossing. Recall that nonsymmorphic space groups contain point group operations coupled with nonprimitive lattice translations.

We illustrate the concept first on a generic minimal model based on the tetragonal CuMnAs AF, considering only the Mn atoms (with one orbital per atom) that form a stack of the crinkled quasi-2D square lattices shown in Figs. 1(b) and 1(c). We first neglect the coupling between these quasi-2D planes; their distance is larger than the first and second nearest-neighbor distances within the quasi-2D plane. The corresponding model Hamiltonian in the crystal momentum space,

$$H_{\mathbf{k}} = -2t\tau_x \cos \frac{k_x}{2} \cos \frac{k_y}{2} - t'(\cos k_x + \cos k_y) + \lambda\tau_z(\sigma_y \sin k_x - \sigma_x \sin k_y) + \tau_z J_n \boldsymbol{\sigma} \cdot \mathbf{n}, \quad (1)$$

consists of the first nearest-neighbor hopping  $t$  (intersublattice  $A$ - $B$  hopping), the second nearest-neighbor hopping  $t'$  (intrasublattice  $A$ - $A$  hopping), the second-neighbor SOC of strength  $\lambda$  [14], and the AF exchange coupling of strength  $J_n$ . The wave vector  $k_{x(y)}$  is in units of the inverse lattice constant,  $\mathbf{n}$  is the Néel vector, and  $\boldsymbol{\tau}$  and  $\boldsymbol{\sigma}$  are Pauli matrices describing the crystal sublattice  $A$ ,  $B$  and spin degrees of freedom, respectively. We diagonalize  $H$  analytically,

$$E_{\mathbf{k}\pm} = -t'(\cos k_x + \cos k_y) \pm \left[ 4t^2 \cos^2 \frac{k_x}{2} \cos^2 \frac{k_y}{2} + (J_n n_x - \lambda \sin k_y)^2 + (J_n n_y + \lambda \sin k_x)^2 + J_n^2 n_z^2 \right]^{1/2}, \quad (2)$$

and plot in Fig. 1(e) the resulting bands measured from the Fermi level for  $\lambda = 0.8t$ ,  $J_n = 0.6t$ , and  $t' = 0.08t$ . For the Néel vector  $\mathbf{n} \parallel [100]$ , we found two DPs  $D_1$  and  $D_2$  in the first BZ along the  $MX$  axis at wave vectors  $\mathbf{D}_1 = [\pi, \arcsin(J_n/\lambda)]$  and  $\mathbf{D}_2 = [\pi, \pi - \arcsin(J_n/\lambda)]$ , as shown in Figs. 1(d) and 1(f).

For the minimal quasi-2D model of the CuMnAs AF, we can now show explicitly that the DPs are protected by a nonsymmorphic, glide mirror plane symmetry [32],  $\mathcal{G}_x = \{M_x | \frac{1}{2}00\}$ . It combines the mirror symmetry  $M_x$  along the  $(100)$  plane with the half-primitive cell translation along the  $[100]$  axis [see Fig. 1(c)] and has eigenvalues  $g_{\pm} = \pm i$ . The fourfold degenerate DP originates from a crossing of two Kramers pairs where the two bands in each pair are degenerate due to the  $\mathcal{PT}$  symmetry. Hybridization between the pairs is prohibited; i.e., the crossing is protected by  $\mathcal{G}_x$  when the following conditions are met. (i) The crossing occurs at the BZ submanifold invariant under  $\mathcal{G}_x$ . This is fulfilled in the  $k_x = 0, \pm\pi$  planes. (ii) The two bands forming a given Kramers pair with the corresponding wave functions  $\psi_{\mathbf{k}}$  and  $\mathcal{PT}\psi_{\mathbf{k}}$  can be assigned

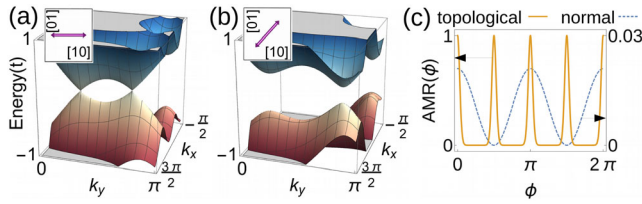


FIG. 2. Topological MIT in our minimal model driven by Néel vector reorientation from (a) [100] to (b) [110] by the Néel SOT. (c) Schematics of the corresponding angular dependence of the topological AMR contrasted to the normal AMR.

the same eigenvalue of  $\mathcal{G}_x$ . From the commutation relation of  $\mathcal{G}_x$  and  $\mathcal{PT}$ , we obtain that this condition is fulfilled only at the BZ submanifold  $k_x = \pm\pi$  [cf. Figs. 1(d) and 1(e)]. (iii) One Kramers pair corresponds to one eigenvalue and the other Kramers pair to the opposite eigenvalue of  $\mathcal{G}_x$ . This can be verified by employing the  $k \cdot p$  perturbation theory. Around, e.g., the  $D_1$  point in the  $k_x = \pi$  plane, we obtain  $E_{D_1+k_y, \pm} = \pm \hbar v_{F,y} k_y$  with the two Kramers pairs fulfilling  $\mathcal{G}_x \psi_{\mathbf{k}\pm} = \mathcal{G}_x \mathcal{PT} \psi_{\mathbf{k}\pm} = \mp i \psi_{\mathbf{k}\pm}$ . This is highlighted in the inset of Fig. 1(e).

Because of the combined  $\mathcal{PT}$  symmetry, we can define the topological index of our DPs analogously to the paramagnetic Dirac semimetals [33]. The topological index  $N(k_y)$  at the crystal momentum  $k_y$  invariant under  $\mathcal{G}_x$  is given by  $N(k_y) = [N_{+i}^C(k_y) - N_{+i}^V(k_y)] - [N_{-i}^C(k_y) - N_{-i}^V(k_y)]$ . Here,  $N_{\pm i}^{C(V)}(k_y)$  is the number of conduction (valence) bands at  $k_y$  with the eigenvalue  $g_{\pm} = \pm i$ . An integer value and a discontinuity of the topological index when crossing the DP in our model is highlighted in the inset of Fig. 1(e). The corresponding topological charge at, e.g., the DP  $D_1$  obtained by approaching  $\mathbf{D}_1$  from left and right [33] is  $Q \equiv [N(\mathbf{D}_1 + \delta) - N(\mathbf{D}_1 - \delta)]/8 = -1$ .

Following the symmetry analysis of Néel SOTs in Refs. [8,29], we obtain for our model AF that the lowest-order ( $\mathbf{n}$ -independent) component of  $\delta s_{A,B}$  is staggered; i.e., it can generate an efficient fieldlike SOT. The field allows for the rotation of  $\mathbf{n}$  in the (001) plane in the direction perpendicular to the applied in-plane current. In Figs. 1(d) and 1(e), we show that for  $\mathbf{n} \parallel [010]$  the DPs move to the  $M'Y$  axis. They are now protected by the  $\mathcal{G}_y = \{M_y | 0 \frac{1}{2} 0\}$  symmetry, as expected for the square quasi-2D lattice.

At intermediate in-plane angles, no DP protecting symmetry remains, and the entire spectrum is gapped [see the  $\mathbf{n} \parallel [110]$  bands in Fig. 1(e)]. As highlighted on the full spectra of the minimal quasi-2D model in Figs. 2(a) and 2(b), this leads to the topological MIT driven by the Néel vector reorientation. The band gap at the DP is a continuous function of the in-plane Néel vector angle  $\Delta(\mathbf{D}_1) \sim J_n \sqrt{1 - \cos(\phi)}$ , where  $\phi$  is measured from the [100] axis. The transport counterpart of the MIT is the topological AMR, which we define as  $\text{AMR} \equiv [\sigma(\phi) - \sigma_{\min}]/\sigma_{\max}$ . Here,  $\sigma(\phi)$

is the  $\phi$ -dependent conductivity with current along the [100] axis and  $\sigma_{\min(\max)}$  referring to the conductivity minimum (maximum). The topological AMR in our Dirac semimetal AF can be extremely large due to the MIT, as illustrated schematically in Fig. 2(c). High AMR values correspond to  $\phi = 0(\pi/2)$  with the closed gap of the DPs at  $MX (M'Y)$ . The mechanism of our topological AMR is based on Fermi surface topology changes induced by staggered order rotations. It is, therefore, fundamentally distinct from the conventional, scattering-related AMR in a normal magnetic metal [34], as we show in Fig. 2(c).

We conclude the discussion of the minimal model AF by taking into account the coupling between the quasi-2D planes. The coupling leads to the following renormalization of the model Hamiltonian (1):  $2t\tau_x \xrightarrow{3D} (2t + t_z \cos k_z)\tau_x + t_z \sin k_z \tau_y$ ,  $t'(\cos k_x + \cos k_y) \xrightarrow{3D} t'(\cos k_x + \cos k_y) + t'_z \cos k_z$ , and  $\lambda \xrightarrow{3D} \lambda - \lambda_z \cos k_z$ . As a result, the  $\mathcal{G}_x$  ( $\mathcal{G}_y$ ) protected DPs in 2D transform into protected nodal lines in 3D. For example,  $\mathbf{D}_1 \xrightarrow{3D} [\pi, \arcsin(J_n/\lambda - \lambda_z \cos k_z), k_z]$  gives an open nodal line for  $\lambda_z < \lambda/2$ , as shown in Fig. 1(f) for  $\lambda_z = 0.2t$ . Note that in our Dirac AF, the nodal lines are dispersive in contrast to the paramagnetic  $J_n = 0$  model [33].

We now verify all observations made in the minimal model by performing full-potential relativistic *ab initio* calculations as implemented in the FLEUR and ELK packages [35]. The exchange correlation potential is parametrized by the Perdew-Burke-Ernzerhof generalized gradient approximation (GGA) [36,37]. The full crystal of tetragonal CuMnAs including also the Cu and As atoms is shown in Fig. 3(a) [38,39]. The results without SOC are summarized in Figs. 3(b) and 3(c). They show the semimetallic character with the dip in the density of states near the Fermi level and numerous band crossings. Note that their position is sensitive to the computational details; as an illustration, we plot in Fig. 3(c) shifted bands obtained in the GGA +  $U$  approximation with the correlation potential  $U = 3$  eV. When SOC is included in the *ab initio* calculations and  $\mathbf{n} \parallel [100]$ , protected nodal lines are obtained in the  $k_x = \pm\pi$  planes, as illustrated in Fig. 3(d). The nodal lines have the open geometry [cf. Fig. 1(f)]. The protection is due to the  $\mathcal{G}_x$  symmetry, also in agreement with the minimal model. Instead of assigning the  $\mathcal{G}_x$  eigenvalues in the complex *ab initio* band structure, we verify this by excluding all other relevant symmetries as the origin of the protection. For  $\mathbf{n} \parallel [100]$ , the space group  $P4/nmm$  of the tetragonal CuMnAs lattice reduces to eight symmetry elements: identity, nonsymmorphic glide planes  $\mathcal{G}_x$  and  $\mathcal{G}_z = \{M_z | \frac{1}{2} \frac{1}{2} 0\}$ , screw axis  $\mathcal{S}_y = \{C_{2y} | 0 \frac{1}{2} 0\}$ , and four  $\mathcal{PT}$  conjugated symmetries. By rotating the Néel vector to  $\mathbf{n} \parallel [110]$  and  $\mathbf{n} \parallel [101]$ ,  $\mathcal{G}_z$  and  $\mathcal{S}_y$  remain symmetries of the AF crystal, respectively. In both cases, however, the nodal lines become gapped, as illustrated in Fig. 3(e), excluding the protection

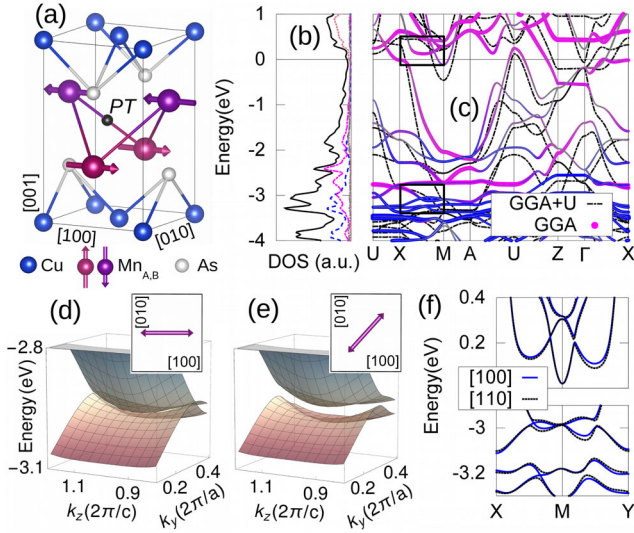


FIG. 3. (a) Crystallographic and magnetic structure of the tetragonal CuMnAs. Atom-resolved (b) density of states with semimetallic pseudogap and (c) band structure without SOC within GGA. GGA +  $U$  shows DPs position shifts. Colors correspond to the atomic colors in (a). Electric control by the Néel SOT of the 3D band dispersion around the nodal line along the  $k_x = \pi$  BZ submanifold calculated by GGA + SOC, which is (d) protected for  $\mathbf{n}||[100]$  by the glide mirror plane and (e) gapped for  $\mathbf{n}||[110]$ .  $a = b \neq c$  are the lattice constants. (f) Cut along the  $XY$  line through the nodal lines at different energies.

by these symmetries. Note that the  $\mathcal{G}_x$  protection makes our tetragonal CuMnAs AF distinct from the earlier identified nonsymmorphic protection in paramagnetic ZrSiS [40].

The fieldlike Néel SOT in the full tetragonal crystal of CuMnAs has the same symmetry as in the minimal model and, therefore, allows for the current-induced rotation of the Néel vector [9,29]. This opens the prospect of electric control of Dirac crossings in an experimentally relevant AF material. However, the tetragonal CuMnAs is not optimal for observing the corresponding topological MIT due to other non-Dirac bands present around the Fermi level [see Fig. 3(c)]. These can be removed, e.g., by lowering the lattice symmetry from tetragonal to orthorhombic [22,24], as we now discuss in the remaining paragraphs.

The nonsymmorphic  $Pnma$  primitive cell of the orthorhombic CuMnAs [41] is shown in Fig. 4(a). It has four Mn sites consisting of the two inversion-partner pairs  $A$ - $B$  and  $A'$ - $B'$ . From the symmetry analysis of the current-induced spin polarizations [29] generated locally at these four sites, we obtain that they contain components which are commensurate with the AF order:  $A$  and  $A'$  sites with one sign of the current-induced spin polarizations belong to one AF spin sublattice, and  $B$  and  $B'$  sites with the opposite sign of the current-induced spin polarizations belong to the opposite AF spin sublattice. This makes the Néel SOT efficient for reorienting AF moments in orthorhombic CuMnAs.

GGA electronic structure calculations without SOC are shown in Figs. 4(b) and 4(c). Consistent with earlier

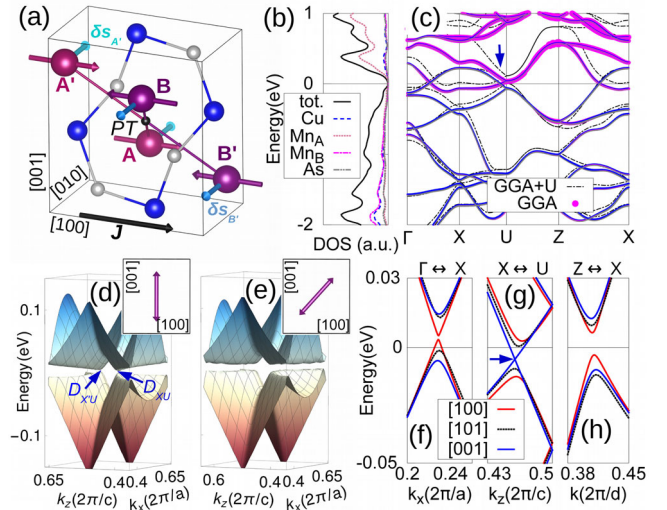


FIG. 4. (a) Crystallographic and magnetic structure of the orthorhombic CuMnAs with Néel SOT spin-polarization  $\delta\mathbf{s}$  for the current  $\mathbf{J}||[100]$ . Atom-resolved (b) point-semimetal density of states and (c) band structure without SOC within GGA. GGA +  $U$  shows DPs position shifts. (d),(e) Topological MIT. Manipulation of the Dirac fermions along the (f)  $\Gamma X$ , (g)  $XU$ , and (h)  $ZX$  axis (units  $d = \sqrt{a^2 + c^2}$  with  $a \neq c$  being the lattice constants) by the Néel SOT from GGA + SOC calculations reveals topological ( $\mathbf{n}||[001]$ ), “trivial” Dirac semimetal ( $\mathbf{n}||[100]$ ), and semiconductor ( $\mathbf{n}||[101]$ ).

reports [22,24], the density of states vanishes at the Fermi level, and we now discuss the properties of the three Fermi level DPs seen in Figs. 4(b) and 4(c). Without SOC, they are part of an ungapped nodal line in the  $k_y = 0$  plane [24]. In the presence of SOC and for  $\mathbf{n}||[001]$ , the DPs along the  $\Gamma X$  and  $ZX$  axes become gapped. The gap opening applies to the entire nodal line, except for the DP along the  $XU$  axis (and also  $X'U$ ), as shown in Figs. 4(d) and 4(f)–4(h). Using the same method as in the *ab initio* calculations for the tetragonal CuMnAs, we identified that the  $XU$  DP protection is due to the screw-axis symmetry  $S_z = \{C_{2z}|\frac{1}{2}0\frac{1}{2}\}$  [24]. The corresponding state at  $\mathbf{n}||[001]$  is then a topological AF Dirac semimetal with the positive topological charge of the  $XU$  DP. For  $\mathbf{n}||[101]$ , all DPs (the entire nodal line) are gapped, and the system becomes an AF semiconductor, as seen in Figs. 4(e)–4(h). Finally, for  $\mathbf{n}||[100]$ , the spin-orbit gap is nearly but not fully closed at the  $\Gamma X$  DP, as shown in Fig. 4(f). This trivial AF Dirac semimetal phase is reminiscent of graphene. Our calculations predict a relatively weak magnetic anisotropy with the equilibrium easy axis along the  $[100]$  direction. Note that the easy-axis determination with  $E_{[001]} - E_{[100]} \sim 0.3$  meV per unit cell is at the resolution limit of our computational method. Since the DPs can appear at the Fermi level [see, also, the comparison of GGA and GGA +  $U$  calculations in Fig. 4(b)], orthorhombic CuMnAs represents a realistic material candidate for observing the topological MIT and AMR driven by the Néel vector reorientation.

We acknowledge support from the grant agency of the Charles University, Grant No. 280815 and of the Czech Republic, Grant No. 14-37427, the Alexander von Humboldt Foundation, EU ERC Synergy Grant No. 610115, and the Transregional Collaborative Research Center (SFB/TRR) 173 SPIN + X. Access to computing and storage facilities owned by parties and projects contributing to the National Grid Infrastructure MetaCentrum provided under the program “Projects of Large Research, Development, and Innovations Infrastructures” (CESNET LM2015042) is greatly appreciated.

- 
- [1] Y. K. Kato, R. C. Myers, A. C. Gossard, and D. D. Awschalom, *Science* **306**, 1910 (2004).
- [2] J. Wunderlich, B. Kaestner, J. Sinova, and T. Jungwirth, *Phys. Rev. Lett.* **94**, 047204 (2005).
- [3] J. Sinova, S. O. Valenzuela, J. Wunderlich, C. H. Back, and T. Jungwirth, *Rev. Mod. Phys.* **87**, 1213 (2015).
- [4] K. S. Novoselov, A. K. Geim, S. V. Morozov, D. Jiang, M. I. Katsnelson, I. V. Grigorieva, S. V. Dubonos, and A. A. Firsov, *Nature (London)* **438**, 197 (2005).
- [5] A. H. Castro Neto, N. M. R. Peres, K. S. Novoselov, A. K. Geim, and F. Guinea, *Rev. Mod. Phys.* **81**, 109 (2009).
- [6] I. M. Miron, K. Garello, G. Gaudin, P.-J. Zermatten, M. V. Costache, S. Auffret, S. Bandiera, B. Rodmacq, A. Schuhl, and P. Gambardella, *Nature (London)* **476**, 189 (2011).
- [7] L. Liu, C.-F. Pai, Y. Li, H. W. Tseng, D. C. Ralph, and R. A. Buhrman, *Science* **336**, 555 (2012).
- [8] J. Železný, H. Gao, K. Výborný, J. Zemen, J. Mašek, A. Manchon, J. Wunderlich, J. Sinova, and T. Jungwirth, *Phys. Rev. Lett.* **113**, 157201 (2014).
- [9] P. Wadley *et al.*, *Science* **351**, 587 (2016).
- [10] X.-G. Wen, *Int. J. Mod. Phys. B* **05**, 1641 (1991).
- [11] M. Z. Hasan and C. L. Kane, *Rev. Mod. Phys.* **82**, 3045 (2010).
- [12] X.-L. Qi and S.-C. Zhang, *Rev. Mod. Phys.* **83**, 1057 (2011).
- [13] A. Bansil, H. Lin, and T. Das, *Rev. Mod. Phys.* **88**, 021004 (2016).
- [14] C. L. Kane and E. J. Mele, *Phys. Rev. Lett.* **95**, 226801 (2005).
- [15] B. A. Bernevig and S.-C. Zhang, *Phys. Rev. Lett.* **96**, 106802 (2006).
- [16] A. Roth, C. Brüne, H. Buhmann, L. W. Molenkamp, J. Maciejko, X.-L. Qi, and S.-C. Zhang, *Science* **325**, 294 (2009).
- [17] C.-Z. Chang *et al.*, *Science* **340**, 167 (2013).
- [18] C.-Z. Chang, W. Zhao, D. Y. Kim, H. Zhang, B. a. Assaf, D. Heiman, S.-C. Zhang, C. Liu, M. H. W. Chan, and J. S. Moodera, *Nat. Mater.* **14**, 473 (2015).
- [19] A. J. Bestwick, E. J. Fox, X. Kou, L. Pan, K. L. Wang, and D. Goldhaber-Gordon, *Phys. Rev. Lett.* **114**, 187201 (2015).
- [20] Y. Fan *et al.*, *Nat. Mater.* **13**, 699 (2014).
- [21] X.-Y. Dong, J.-F. Wang, R.-X. Zhang, W.-H. Duan, B.-F. Zhu, J. O. Sofo, and C.-X. Liu, *Nat. Commun.* **6**, 8517 (2015).
- [22] F. Máca, J. Mašek, O. Stelmakhovych, X. Martí, H. Reichlová, K. Uhlířová, P. Beran, P. Wadley, V. Novák, and T. Jungwirth, *J. Magn. Magn. Mater.* **324**, 1606 (2012).
- [23] L. Šmejkal *et al.*, <http://www.dpg-verhandlungen.de/year/2016/conference/regensburg/part/ma/session/35/contribution/1>. P. Tang *et al.*, <http://www.dpg-verhandlungen.de/year/2016/conference/regensburg/part/o/session/80/contribution/2>.
- [24] P. Tang, Q. Zhou, G. Xu, and S.-C. Zhang, *Nat. Phys.* **12**, 1100 (2016).
- [25] B. A. Bernevig and T. L. Hughes, *Topological Insulators and Topological Superconductors* (Princeton University Press, Princeton, 2013).
- [26] C. Herring, in *Magnetism*, edited by G. T. Rado and H. Suhl (Academic Press, New York, 1966), Vol. IV.
- [27] A. Cracknell, *Magnetism in Crystalline Materials: Applications of the Theory of Groups of Cambiant Symmetry* (Elsevier Science Limited, New York, 1975).
- [28] H. Chen, Q. Niu, and A. H. MacDonald, *Phys. Rev. Lett.* **112**, 017205 (2014).
- [29] J. Železný, H. Gao, A. Manchon, F. Freimuth, Y. Mokrousov, J. Zemen, J. Mašek, J. Sinova, and T. Jungwirth, *Phys. Rev. B* **95**, 014403 (2017).
- [30] Z. Wang, Y. Sun, X. Q. Chen, C. Franchini, G. Xu, H. Weng, X. Dai, and Z. Fang, *Phys. Rev. B* **85**, 195320 (2012).
- [31] S. M. Young, S. Zaheer, J. C. Y. Teo, C. L. Kane, E. J. Mele, and A. M. Rappe, *Phys. Rev. Lett.* **108**, 140405 (2012).
- [32] S. M. Young and C. L. Kane, *Phys. Rev. Lett.* **115**, 126803 (2015).
- [33] B.-J. Yang, T. A. Bojesen, T. Morimoto, and A. Furusaki, [arXiv:1604.00843](https://arxiv.org/abs/1604.00843).
- [34] X. Marti *et al.*, *Nat. Mater.* **13**, 367 (2014).
- [35] <http://elk.sourceforge.net/>; <http://flapw.de>.
- [36] J. P. Perdew, K. Burke, and M. Ernzerhof, *Phys. Rev. Lett.* **77**, 3865 (1996).
- [37] J. P. Perdew, K. Burke, and M. Ernzerhof, *Phys. Rev. Lett.* **78**, 1396 (1997).
- [38] P. Wadley *et al.*, *Nat. Commun.* **4**, 2322 (2013).
- [39] P. Wadley *et al.*, *Sci. Rep.* **5**, 17079 (2015).
- [40] L. M. Schoop, M. N. Ali, C. Straßer, A. Topp, A. Varykhalov, D. Marchenko, V. Duppel, S. S. P. Parkin, B. V. Lotsch, and C. R. Ast, *Nat. Commun.* **7**, 11696 (2016).
- [41] J. J. Mündelein and H. U. Schuster, *Z. Naturforsch. B* **47**, 925 (1992).